Proceedings of the 13th International Forum of Automotive Traffic Safety, 2016,pp443-455
No.ATS.2016.427

Crashing Analysis and Multi-Objective Robust Optimization of a Underframe Structure for High-Speed Trains

Lin Hou[1], Yong Peng[1,2]
[1] *Key Laboratory of Traffic Safety on Track of Ministry of Education, School of Traffic & Transportation Engineering, Central South University, Changsha, 410075, China*
[2] *State Key Laboratory of High Performance Complex Manufacturing, Central South University, Changsha, 410006, China*
Email: yong_peng@csu.edu.cn

Abstract: The deterministic design optimization has been widely used in crashworthiness designs of vehicles. However, the deterministic design is likely to become less meaningful or even unacceptable while taking into account variances of design variables due to the manufacturing deviation. To overcome this shortcoming, a multi-objective robust design optimizationis carried out by employing polynomial response surface models (PRSM), “k-sigma” robust design criteria, Non-Dominated Sorting Genetic Algorithm II (NSGA-II), and Monte Carlo simulations(MCS) technique. The optimization procedure is adopted for the crashworthiness design of the front-end underframe structure used in high-speed trains, where specific energy absorption () and initial peak force () are taken as objectives.MCS points of the robust optimum show that few designs will violate the constraint while taking into account design variables uncertainties, and the 6-sigma robust optimum has the efficient energy absorption capacity while satisfying the design constraint.

Keywords: Multi-objective robust optimization; Monte Carlo simulation; Crashworthiness; Front-end underframe structure

1. Introduction

Crashworthiness of railway vehicles has become an important topic all over the world. Train collision accidents cannot be avoided completely. A collision accident will cause significant casualties and property losses. According to the database of the Federal Railroad Administration (FRA), 76 train passengers died in the United States from 2006 to 2016 [1]. To protect structure integrity of the part of a vehicle occupied by passengers and crew and to reduce injury risk of occupants, the research on crashworthiness of anti-climber structures and energy-absorbing devices has been developed in recent years.

Many studies have been reported in the impact performance of energy-absorbing structures using numerical models and experiment approaches. Crash performance of various structures has been investigated over the past years. Compared with other structures, thin-walled structural members have the capability of desired deformation and high energy absorption efficiency [2-4]. Beik et al. [5] compared crashworthiness of a tapered thin-walled S-shaped structure with internal diagonal reinforcement and the structure without reinforcement, where the reinforcing structure is shown to have a higher energy absorption capacity. Azimi and Asgari [6] proposed a new bi-tubular conical-circular structure to amend the peak crushing load under same energy absorption condition and improve energy absorption characteristics under oblique loading. Peng et al. [7] proposed a composite energy-absorbing structure used in subway vehicles in order to protect passengers and crew from injuries during collision accident.

More importantly, it is of great importance to obtain a crashworthy structure with high energy absorption, low peak force, and progressive deformation simultaneously. The design optimization of structure parameters plays a critical role on designing energy-absorbing devices and structures. Avalle et al. [8] used an iterative optimization algorithm based on a multipoint approximation scheme and the steepest descent method to identify the best geometrical conFigureuration of several energy absorbing devices. Khalkhali et al. [9] conducted a multi-objective optimization to improve the impact performance of perforated square tubes using modified Non-dominated Sorting Genetic Algorithm II (NSGA-II) and Multi-objective Particle Swarm Optimization (MOPSO). Najafi and Rais-Rohani [10] presented a multi-objective optimization of thin-walled double-hat magnesium alloy tubes. The optimization results showed the importance of retaining material history effects for more accurate prediction of performance characteristics. Duddeck et al. [11] proposed a special approach based on Hybrid Cellular Automata, which is able to derive optimal topologies for thin-walled structures for crashworthiness. However, these above mentioned studies are restricted on deterministic optimization without taking into account uncertainties of design parameters exist in real-life applications. Optimized deterministic designs are usually close to constraints, which may lead to catastrophic failure of vehicle energy absorbers during train crash incidents.

In this study, a finite element (FE) model of a front-end underframe structure is constructed and validated through dynamic impact experiment. Deterministic and robust design optimizations are implemented to obtain optimal designs of the underframe structure. The Optimal Latin Hypercube Design (Opt LHD) method is adopted to generate sampling points. Based on these samples, polynomial response surface models (PRSM) used in multi-objective optimization are constructed for objective responses. The Non-Dominated Sorting Genetic Algorithm II (NSGA-II), “k-sigma” robust design method, and Monte Carlo simulations (MCS) technique are employed to obtain Pareto optimal fronts for the front-end underframe structure.

2. Experimental setups

2.1 Details of the structure

As shown in Figure. 1, the new front-end underframe structure is a symmetrical centre sill-cross beam component. For the structure, a vertical plate, a horizontal plate, and a side plate with a rounded corner of 17 mm constitute the centre sill (length of 1800 mm) with an approximate rectangular cross-section. There are three cross beams connected to the two centre sills in the transverse direction. The cross beam is composed of two beams (vertical and horizontal) with the same length (508 mm) and thickness (10 mm). In the longitudinal direction, the ends of the centre sill connect the frontal closing plate with a cross-section of 192 mm × 189 mm and the bolt seat with a cross-section of 400 × 400 mm, respectively. There are weld lines combine centre sills and bolt seats in the real structure. In the simulation model, weld lines were simulated using sharing nodes method. To improve the crashworthiness of the structure, there is a diagonal closing plate attaches the three plates inside the centre sill. During an initial stage of collision process, a high-speed train stores tremendous kinematic energy. The stiffness of the frontal contact area of the front-end underframe structure should be enough to resist the huge initial impact force and provide support for the controllable deformation of centre sills. The wall thicknesses of the vertical cross beam, horizontal cross beam, frontal closing plate, vertical plate of centre sill, horizontal plate of centre sill, side plate of centre sill, and diagonal closing plate are 10 mm, 10 mm, 8 mm, 8 mm, 11 mm, 10 mm, and 8 mm, respectively.

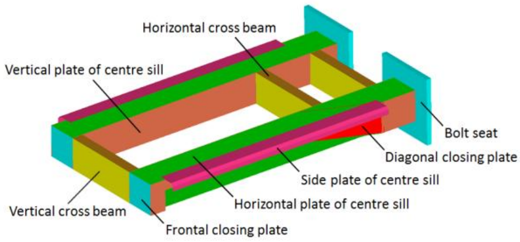

Figure. 1 Front-end underframe structure

2.2 Experimental details

To obtain the mechanical properties of the aluminum material, quasi-static tensile experiments were carried out on standard material specimens [12] cut from the same front-end underframe structure. The profile dimensions of machined experimental specimens used in quasi-static tensile tests are depicted in Figure. 2, where L0, Lc, and Lt represent the original gauge length, parallel length, and overall length of the test specimen, respectively. As shown in Figure. 3, quasi-static tensile tests with a rate of 10.0 mm/min were conducted using a universal material testing system (MTS 647) hydraulic wedge grip tension experiment machine. Three true stress-strain curves of the material in Figure. 4 are determined by the force-displacement behavior obtained in tensile tests. Table 1 lists parameters for mechanical properties of the aluminum material using the mean value of these three curves.

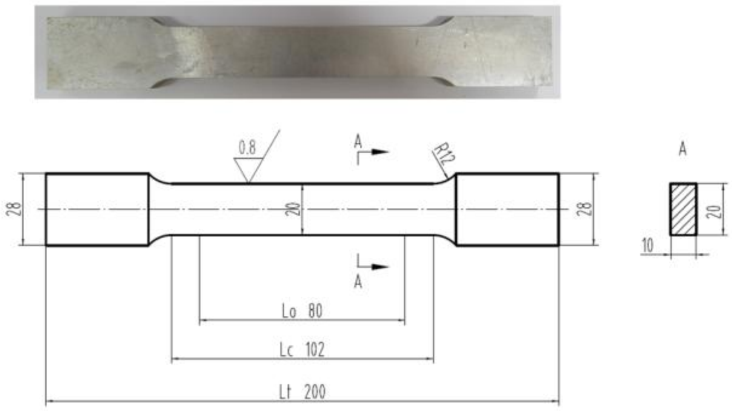

Figure. 2 Profile dimensions of the standard tensile test specimen

Figure. 3 Quasi-static tensile test condition

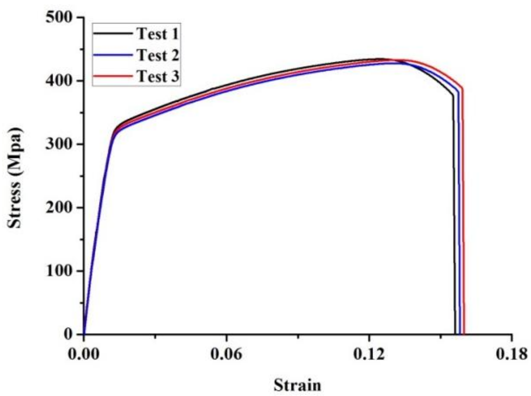

Figure. 4True stress-strain curve under the quasi-static loading test

Table 1 Material parameters of the front-end underframe structure

Parameters	Units	Value
Density	Kg/m^3	2650
Poisson’s ratio	-	0.3
Yong’s modulus	MPa	28000
Yield stress	MPa	323
Ultimate tensile strength	MPa	434

To obtain the collision performance of the front-end underframe structure, a full-scale dynamic crash experiment on the structure was conducted using a test trolley with the mass of 26.01 t, as shown in Figureure. 5. The front-end underframe structure is fixed on the test trolley by sixteen bolts to restrict movements of the structure completely. The impact trolley and the structure were accelerated to an initial velocity of 4.14 m/s (14.904 km/h) to crash into a rigid wall using a power transmission system provided by an electric motor. The impact velocity of the experimental specimen was measured by a laser velocimeter, which was located in the center line of tracks and close to the fixed rigid wall. Four force sensors were installed on the rigid wall to measure the impact force in real time uniformly. To guarantee the test precision and prevent the level of measured force from exceeding the test range, the range of each force sensor was set to 700 kN. Two high-speed cameras were placed on the side of the front-end underframe structure to capture the deformation process of the structure. Then, the dynamic behaviors, such as the time histories of the stroke and the velocity can be analyzed in terms of the obtained data from high-speed cameras.

Figure. 5Dynamic collision experimental set-up

2.3 Numerical model

2.3.1 Definition of the collision simulation model

In this study, the explicit nonlinear finite element (FE) code LS-DYNA was used to conduct the FE numerical simulation analysis. As shown in Figure. 6, the FE model comprises these four components: fixed rigid wall, front-end underframe structure, test trolley, and tracks. The Belytschko-Tsay shell element that includes two integration points through the thickness and one integration point in the element plane is employed to model the thin-walled structural members, such as cross beams and centre sills of the underframe structure. For relatively thick and rigid components, such as bolt seats, were defined using constant stress solid elements.

To balance the inconsistency of high accuracy and simulation efficiency, the mesh size of 5 mm was applied for the shell element and 10 mm for the solid element. The fourth hourglass control stiffness formula with a coefficient of 0.05 was selected to avoid hourglass energy in the simulation analysis. The self-contact of the front-end underframe structure adopted the “AUTOMATIC_SINGLE_SURFACE” contact algorithm and the “NODES_TO_SURFACE” contact algorithm. The “AUTOMATIC_SURFACE_TO_SURFACE” contact algorithm was applied to the contact between the front-end underframe structure and the rigid wall. The static coefficient of contact friction was defined as 0.3, while the dynamic coefficient of contact friction was set as 0.1 [7, 13]. The gravity acceleration was defined as 9.81 m/s2 to apply for the FE model. The six degrees of freedom of tracks were fully constrained.

To keep consistent with the experimental set-up, the front-end underframe structure was fixed on the front end of a crashing test trolley with a collision velocity of 4.14 m/s to impact a rigid wall.

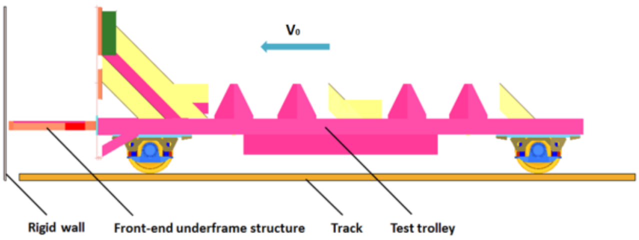

Figure. 6FE model and simulation conditions

2.3.2Material model

Centre sills and cross beams of the front-end underframe structure was modeled by the material model, *MAT.024_PIECEWISE_LINEAR_PLASTICITY, whose mechanical properties were obtained from the quasi-static tensile experimental data (see Figure. 4 and Table 1). The property of the “MAT_PLASTIC_KINEMATIC” was used to model bolt seats structures. The Cowper-Symonds model was used to model the material in consideration of the strain rate effect for a low strain rate condition [14]. In this model, the constitutive relationship of the material can be describing by the following equation:

$$\sigma_y = \left[1 + \left(\frac{\dot{\varepsilon}}{C}\right)^{1/P}\right]\left(\sigma_0 + \beta E_p \varepsilon_{eff}^{p}\right) \quad (1)$$

$$E_p = E_{tan} E/(E - E_{tan}) (2)$$

where is the yield stress; is the strain rate; and are strain rate parameters of the Cowper-Symonds model; is the initial yield stress; is the hardening parameter changes from 0 to 1, corresponding to kinematic and isotropic hardening, respectively; is the plastic hardening modulus; is the equivalent plastic strain; is the Yong’s modulus; is the tangent modulus of the plastic deformation. Base on the literature [7], =40 s-1, =5, and =1. Parameters for mechanical properties of the aluminum material are shown in Table 1.

2.3.3Evaluation indicators of crashworthiness

The objective of design and optimization for an underframe structure is to obtain a controllable deformation process, the minimum peak crushing force, and the maximum strain energy absorption during a collision [15]. Some key indexes, such as the crashing duration time (), crashing compressive stroke (), initial peak force (), mean crashing force (), and energy absorption (), are widely adopted to evaluate the impact performance of an underframe structure [16-17].

An initial peak force will generate a harmful collision deceleration to cause injuries for passengers. The lower the peak force, the higher the safety. As a critical index, the energy absorption is adopted to analyze the energy-absorption capacity of a structure, and the is expected to be maximized during the deformation of a structure. The energy absorption can be obtained by the following formula:

$$E_p = E_{tan} E/(E - E_{tan}) \qquad (3)$$

where is the instantaneous crushing force with a function of the compressive stroke .

The specific energy absorption () measures the absorbed energy in a unit structural mass as:

$$SEA = \frac{EA}{m}(4)$$

The mean crashing force for a determinate stroke also assesses the capacity of the energy absorption of a structure. The can be defined as divided by the compressive stroke :

$$F_{avg} = \frac{EA}{S} \qquad (5)$$

2.4 Validation of the FE model

To assess the collision behavior of the front-end underframe structure and evaluate the accuracy of the FE model, simulation results of the force-time history curve, stroke-time history, and deformation pattern of the numerical model are compared with the test results under identical boundary conditions.

Figure. 7 depicts experiment and simulation results of resulting force-time history response curves. The simulation result shows good consistency with the experiment during the entire crash duration time. The plastic deformation performance of the structure is well predicted by the FE model. At 5.85 ms and 6.25 ms, impact forces rise to initial peak values of 2.6152×103 kN and 2.5337×103 kN for experiment and simulation, respectively. Crashing forces of the test and simulation drop to zero essentially simultaneously, and the duration time are 133 ms and 135 ms respectively. Considering the complexity of experimental conditions, the force-time response of simulation cannot be absolutely agree with the experiment. Figure. 8 indicates stroke-time curves for experiment and simulation results. The stroke values reach to maximum of 217.74 mm and 218.19 mm at the time of 112 ms and 117 ms for experiment and simulation, respectively. At 133 ms and 135 ms, the stroke of the test and simulation are 211.92 mm and 212.47 mm, respectively. The stroke-time response curve of the simulation agrees well with the experiment. Moreover, the mean crashing force and energy absorption are 0.8317×103 kN, 0.1762×103 kJ and 0.8253×103 kN, 0.1753×103 kJ for experiment and simulation respectively.

Furthermore, the deformation process of the simulation result should also be compared with the experiment. The deformation mode of the front-end underframe structure in experiment was obtained by the left high-speed camera with the frame rate of 10,000 frames per second. Figure. 9 shows the comparison of deformation series of the structure for the experiment and simulation. The deformation process of the underframe structure for simulation is in good agreement with the experiment result. The horizontal, vertical, and side plates of centre sills of the structure undergo plastic bending and stretching and form inward and outward folds during the crush process. At 0 ms, the front-end vertical cross beam of the structure impacted the rigid wall initially. The upper horizontal and side plates of centre sills bent downwards at 10 ms, while the nether horizontal plates bent upwards. Simultaneously, the vertical plates started to bent inwards at the initial stage of the impact. The crash process of the structure lasted nearly 130 ms, which correspond to the duration time of the impact force. The crash process finished when the velocity of the test trolley and structure dropped to zero (i.e., the kinetic energy of the system decreased to zero), and the system moved away from the fixed rigid wall. By verification, the FE model can be adopted in the next optimization design based on its accuracy.

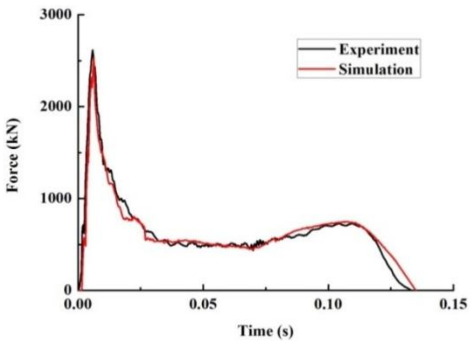

Figure. 7Resultant force-time curves for experiment and simulation

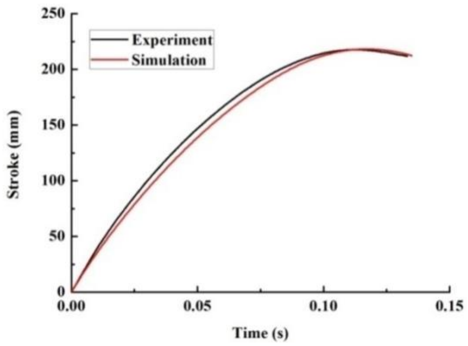

Figure. 8 Stroke-time curves for experiment and simulation

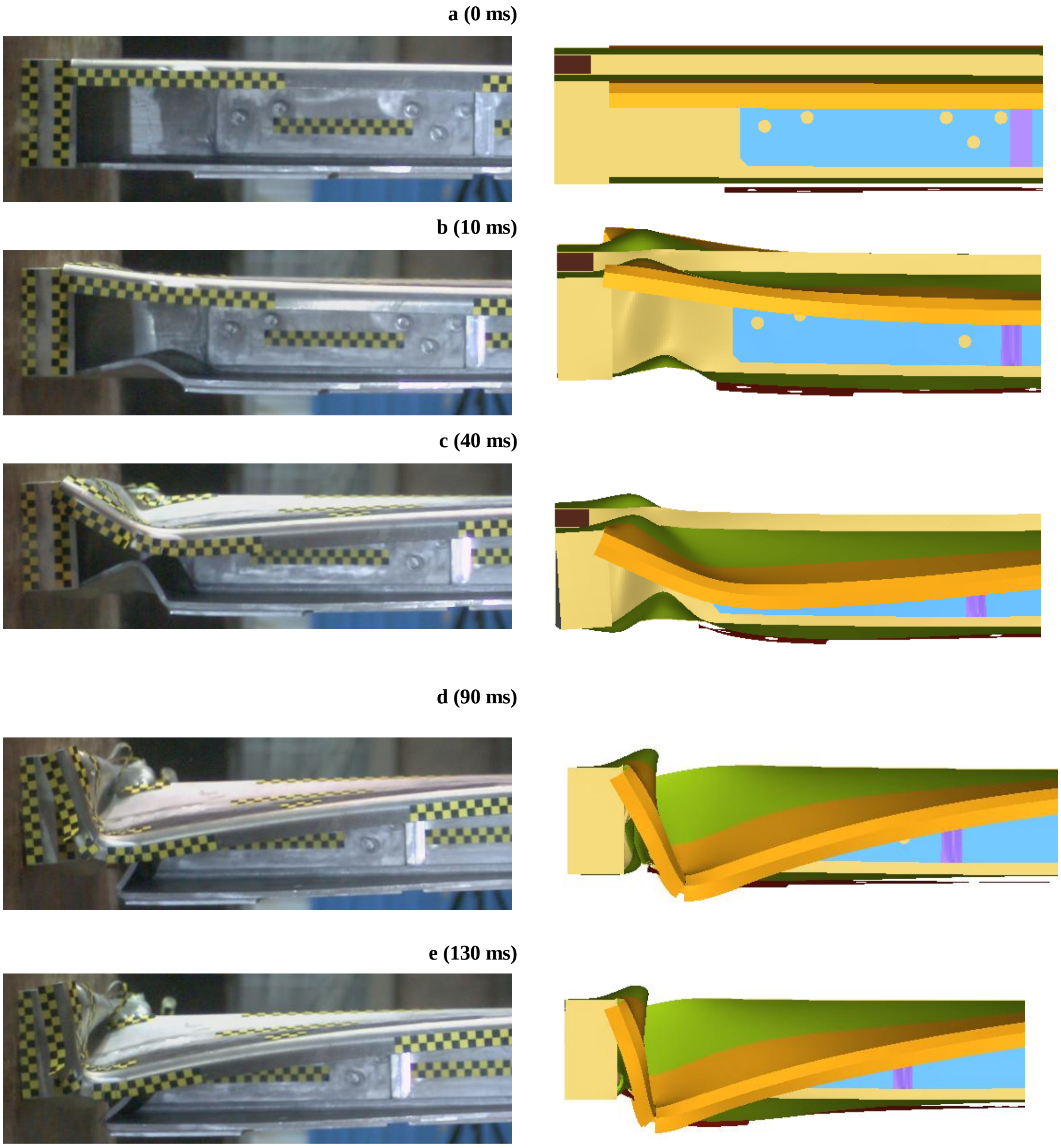

Figure. 9 Comparison of results of deformation pattern for the test and simulatio

3. Multi-objective optimization methodology

3.1 Design of experiment (DOE)

The Optimal Latin Hypercube Design (Opt LHD) is applied to generate sampling points for the design of experiment (DOE). Figure. 10 plots the design matrix including 20 sample points obtained by the Opt LHD.

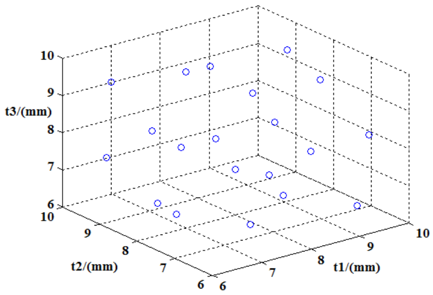

Figure. 10 Distribution of sample points derived by the Opt LHD

3.2 Metamodel (surrogate model) and error metrics

The polynomial response surface model (PRSM) is employed to obtain mathematical objective functions for SEA and Fp of the structure. The response surface model can be described as the Eq. (6). Figure. 11 illustrates the process of establishing a surrogate model.

$$f(x) = \sum_{i=1}^{n} a_i \beta_i(x) \tag{6}$$

where denotes the predicted response, which determined by a group of basic functions. denotes adjust coefficients derived using the least-square method. represents basic functions, and represents the number of basic functions.

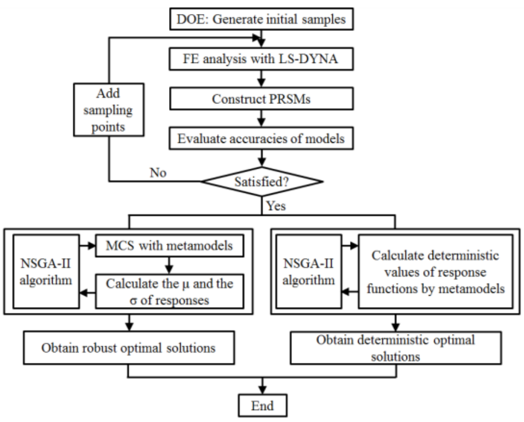

Figure. 11 The process of multi-objective deterministic and robustoptimization design

3.3 Monte Carlo simulation (MCS)

The Monte Carlo simulation (MCS) technology is implemented in this study to compute the probability distribution of response performance. Some random samples are obtained from a certain distribution of input parameters and corresponding output responses for these samples can be derived using functional evaluations. The probability distribution characteristic of output values is generated by conducting the statistical analysis on outputs. According to Monte Carlo simulation, the mean value () of a function is obtained as:

$$\mu[f(x)] = \frac{1}{N}\sum_{i=1}^{N} f(x_i) \qquad (7)$$

where denotes the vector of random variables, stands for the th sample point obtained from a statistical distribution, and is the number of all random sample points obtained. Moreover, the standard deviation (σ) of a function is calculated as:

$$\sigma[f(x)] = \sqrt{\frac{1}{N-1}\sum_{i=1}^{N}(f(x_i) - \mu[f(x_i)])^2} \quad (8)$$

3.4 Definition of multi-objective robust optimization problems

Considering the existence of uncertainties of design variables, the robust optimization is employed in the design of the front-end underframe structure. Both the mean value and the standard deviation of response values are calculated in the multi-objective robust optimization. The mathematical model of a typical "-sigma" multi-objective robust optimization problem can be described as [18-20]:

$$\begin{cases} \text{Min.} \quad \mu[f_i(x)] + k\sigma[f_i(x)] & i = 1,2,\ldots,M \\ \text{s.t.} \quad \mu[g_j(x)] + k\sigma[g_j(x)] \le 0 & j = 1,2,\ldots,N \\ \qquad x^L + k\sigma[x] \le \mu[x] \le x^U - k\sigma[x] & \end{cases} \qquad (9)$$

where and represent the mean value and the standard deviation of the th objective function, respectively. and denote the mean value and the standard deviation of the th constraint function, respectively. and are the mean value and the standard deviation of the design variable . represents the robustness level. The value of usually equals to 1.285, 3 or 6 (mean 1.285-sigma, 3-sigma or 6-sigma), and the corresponding probability of meeting the constraint is 90% (=1.285), 99.73% (=3) or 99.9999998% (=6), respectively. As shown in Figure. 11, the multi-objective robust design optimization problem is solved by a procedure which implements surrogate models, the Non-Dominated Sorting Genetic Algorithm II (NSGA-II), the "-sigma" robust method and the MCS technique.

3.5 Multi-objectivegeneticalgorithm

Optimal solutions can be determined rapidly in the design space by genetic algorithm, which has an excellent global search capability. The Non-Dominated Sorting Genetic Algorithm II (NSGA-II) is used to generate optimal solution set (Pareto front) in this study. Parameter details of the NSGA-II algorithm are defined in Table 2.

Table 2 Parameter details of the NSGA-II algorithm

Parameters	Value
Population size(multipleof4)	20
Numberofgenerations	100
Crossoverprobability	0.9
Crossoverdistributionindex	10
Mutation distributionindex	20
Initialization mode	Random
Max failedruns	5
Failedrunpenaltyvalue	1.0E30
Failedrunobjectivevalue	1.0E30

4. Multi-objective robust optimization results and discussion

In this study, the optimization problem can be described as: using the thickness of the vertical plate of centre sill, the horizontal plate of centre sill, and the side plate of centre sill as design variables , , and , respectively. The and the are design objectives in the optimization problem. To take into account effects of uncertainties, the 6-sigma (6-σ) based robust design optimization method is implemented in this study. Design variables , , and are considered as random variables which are assumed to distribute normally as shown in Table 3 from manufacturing perspectives [21]. The 6-sigma based robust optimization problem can be described mathematically as:

$$\begin{cases} \mathrm{Min.} -\mu[\mathrm{SEA}(t_1,t_2,t_3)] + 6\sigma[\mathrm{SEA}(t_1,t_2,t_3)], \\ \mu[F_p(t_1,t_2,t_3)] + 6\sigma[F_p(t_1,t_2,t_3)] \\ \mathrm{s.t.}\ 6\ \mathrm{mm} + 6\sigma[t_1] \le \mu[t_1] \le 10\ \mathrm{mm} - 6\sigma[t_1] \\ 6\ \mathrm{mm} + 6\sigma[t_2] \le \mu[t_2] \le 10\ \mathrm{mm} - 6\sigma[t_2] \\ 6\ \mathrm{mm} + 6\sigma[t_3] \le \mu[t_3] \le 10\ \mathrm{mm} - 6\sigma[t_3] \end{cases} \tag{10}$$

Table 3Probabilistic characteristic of random variables

Variable	Mean (μ)	Standard deviation (σ)	Distribution
		2% of	Normal
		2% of	Normal
		2% of	Normal

Table 4Pareto optimal solutions obtained with constraints of

Objective		$\le 1.1\times10^3$ kN
Design variables	(mm)	6
	(mm)	6.11
	(mm)	6.11
(10^3 kN)	Metamodel	1.0869
	FEA	1.0865
	Error (%)	0.03
(kJ/kg)	Metamodel	-1.1734
	FEA	-1.1454
	Error (%)	2.4

In this study, probability parameters of design variables and objective responses are same (i.e. k=6 for design variables and objective responses). Figure. 12 depicts the Pareto optimal set of the design optimization for 6-sigma. As shown in Figure. 12, the solid black circle represents the optimal design of the multi-objective robust optimization with 6-sigma with maximal value while ≤1.1×103 kN.

Table 4 also summarizes design variables of the robust optimal solution. The FE model of the underframe structure after robust optimization is established and corresponding and values are validated by FE simulation. The relative error of the metamodel is less than 3%. In addition, results shown in Figure. 12 indicate that the Pareto optimal front of 3-sigma robust optimization has a good consistency with the 6-sigma design optimization and two Pareto optimal designs are close significantly, which demonstrates the 3-sigma design optimization may be sufficient to obtain a reliable solution in practical engineering design.

All Pareto optimal sets in Figure. 12 are generated with the same population size of 20 and generations of 100. Pareto fronts in these design optimizations illustrate the trade-off between the specific energy absorption and the initial peak force . These two objective responses strongly compete against each other, the more the , the higher the , which indicates that a compromise must be conducted between the energy absorption and the peak force. Compared with the deterministic design optimization, ranges of Pareto fronts in robust design optimization change significantly, Pareto sets of robust optimizations are to the right side of the corresponding Pareto set of the deterministic optimization. As shown in Figure. 12, variances of design variables in robust design optimization have a lower likelihood to violate constraints, and the Pareto optimal solution is more reliable and stable. However, the objective performance of energy absorption capacity has to sacrifice. Therefore, a compromise should be made between the objective robustness and performance.

To testify the robustness of the robust optimal design, 5,000 MCS points are generated by the normal distribution [21] to obtain solutions around the 6-sigma robust optimum, as plotted in Figure. 13. Figure. 13 shows the comparison of the 6-sigma robust optimum and the respective deterministic optimum. The clouds of black dots denote normally distributed point around the 6-sigma robust optimum. Almost all MCS points around the robust optimum are below the constraint of ≤1.1×103 kN, and the loss of objective performance caused by the perturbation of design variables in robust design optimization can be accepted. However, the deterministic optimal solution in Figure. 13 is close to the specified constraint of the . The variance of design variables may lead to the solution to exceed the limit value, which demonstrates that the robustness of the robust optimal design is relatively higher. It should be pointed out that the increase of the robustness will lead to the decrease of the value, as shown in Figure. 13. However, the 6-sigma robust optimum has the efficient energy absorption capacity while satisfying the design constraint. Therefore, the robust optimal design of the front-end underframe structure can be used in practical engineering applications.

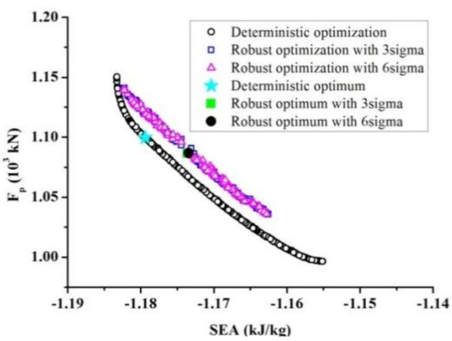

Figure. 12 Comparison of Pareto optimal fronts in the multi-objective deterministic optimization and multi-objective robust optimizations

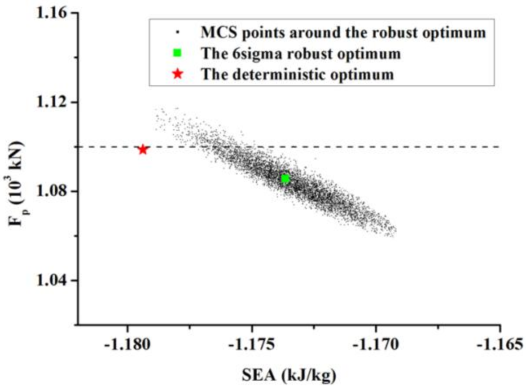

Figure. 13MCS points and Pareto optimal solutions with constraint by metamodels

5. Conclusions

In this study, the numerical simulation analysis of the front-end underframe structure used in high-speed trains is performed and validated by dynamic impact experiment. The comparison between numerical and experimental results demonstrates a good agreement.

Based on the verified FE model, the multi-objective robust optimization is carried out by employing polynomial response surface models, sigma criteria, NSGA-II algorithm, and MCS technique, which allows considering effects of design variables uncertainties on objective performance. The optimization procedure is proved effective in the crashworthiness design for the front-end underframe structure, where specific energy absorption and initial peak force are taken as objectives. MCS points of the robust optimum show that few designs will violate the constraint while taking into account design variables uncertainties. The 6-sigma robust optimum has the efficient energy absorption capacity while satisfying the design constraint. The robust optimal design of the front-end underframe structure can be used in practical engineering applications.

Acknowledgments

The work was supported from the National Natural Science Foundation of China (51405517, U1334208), the Natural Science Foundation of Hunan (2015JJ3155) and the China Postdoctoral Science Foundation (2015M570691).

References

[1] Federal Railroad Administration (2016) Railroad Safety Data: Casualty Summary Tables.
[2] Al Galib D, Limam A (2004) Experimental and numerical investigation of static and dynamic axial crushing of circular aluminum tubes. Thin Wall Struct 42:1103-1137
[3] Abramowicz W (2003) Thin-walled structures as impactenergy absorbers. Thin Wall Struct 41:91-107
[4] Xie S, Zhou H (2014) Impact characteristics of a composite energy absorbing bearing structure for railway vehicles. Compos Part B-Eng 67:455-463
[5] Beik V, Fard M, Jazar R (2016) Crashworthiness of tapered thin-walled S-shaped structures Thin Wall Struct 102:139-147
[6] Azimi MB, Asgari M (2016) A new bi-tubular conical–circular structure for improving crushing behavior under axial and oblique impacts. Int J Mech Sci 105:253-265
[7] Peng Y, Deng W, Xu P, Yao S (2015) Study on the collision performance of a composite energy-absorbing structure for subway vehicles. Thin Wall Struct 94:663-672
[8] Avalle M, Chiandussi G, Belingardi G (2002) Design optimization by response surface methodology: application to crashworthiness design of vehicle structures. Struct Multidisc Optim 24:325-332
[9] Khalkhali A, Mostafapour M, Tabatabaie SM, Ansari B (2016) Multi-objective crashworthiness optimization of perforated square tubes using modified NSGAII and MOPSO. Struct Multidisc Optim 54:45-61
[10] Najafi A, Rais-Rohani M (2012) Sequential coupled process-performance simulation and multi-objective optimization of thin-walled tubes. Mater Des 41:89-98
[11] Duddeck F, Hunkeler S, Lozano P, Wehrle E, Zeng D (2016) Topology optimization for crashworthiness of thin-walled structures under axial impact using hybrid cellular automata. Struct Multidisc Optim doi:10.1007/s00158-016-1445-y
[12] State Standard of the People's Republic of China (2009) Metallic materials-Tensile testing-Part 1: Method of test at

room temperature.
[13] Xu P, Yang C, Peng Y, Yao S, Zhang D, Li B (2016) Crash performance and multi-objective optimization of a gradual energy-absorbing structure for subway vehicles. Int J Mech Sci 107:1-12
[14] DietenbergerM,BuyukM,KanCD (2005) Developmentofahighstrain-ratedependentvehiclemodel.Bamberg:NationalCrashAnalysisCenterVirginia
[15] White MD, Jones N(1999)Experimentalquasi-staticaxialcrushingoftop-hatanddouble-hat thin-walledsections. Int J Mech Sci41:179–208
[16] Tarigopula V, Langseth M, Hopperstad OS, Clausen AH (2006) Axial crushing of thin-walled high-strength steel sections. Int J Impact Eng 32:847-882
[17] Kazancı Z, Bathe KJ (2012) Crushing and crashing of tubes with implicit time integration. Int J Impact Eng 42:80-88
[18] Zhu P, Zhang Y, Chen GL (2009) Metamodel-based lightweight design of an automotive front-body structure using robust optimization. P I Mech Eng D-J Aut 223:1133-1147
[19] Baril C, Yacout S, Clément B (2011) Design for Six Sigma through collaborative multiobjective optimization. Comput Ind Eng 60:43-55
[20] Sun G, Li G, Zhou S, Li H, Hou S, Li Q (2010) Crashworthiness design of vehicle by using multiobjective robust optimization. Struct Multidisc Optim 44:99-110
[21] Li F, Sun G, Huang X, Rong J, Li Q (2015) Multiobjective robust optimization for crashworthiness design of foam filled thin-walled structures with random and interval uncertainties. Eng Struct 88:111-124